Quantitative structural assessment of heterogeneous catalysts by electron tomography

Roman Grothausmann[*a]　　　Gerald Zehl[a]　　　Ingo Manke[a]　　　Sebastian Fiechter[a]

Peter Bogdanoff[a]　　　Iris Dorbandt[a]　　　Andreas Kupsch[b]　　　Axel Lange[b]

Manfred P. Hentschel[b]　　　Gerhard Schumacher[a]　　　John Banhart[a]

14th September 2011

HZB Helmholtz-Zentrum Berlin GmbH, Hahn-Meitner-Platz 1, 14109 Berlin, Germany
BAM Federal Institute for Materials Research and Testing, 12200 Berlin, Germany
* Corresponding author: roman.grothausmann@helmholtz-berlin.de

Abstract

We present transmission electron microscope (TEM) tomography investigations of ruthenium-based fuel cell catalyst materials as employed in Direct Methanol Fuel Cells (DMFC). The digital three-dimensional representation of the samples does not only enable detailed studies on number, size and shape, but also on the local orientation of the ruthenium particles to their support and their freely accessible surface area. The shape analysis shows the ruthenium particles deviate significantly from spherical symmetry which increases their surface to volume ratio. The morphological studies help to understand the structure formation mechanisms during the fabrication as well as the high effectiveness of these catalysts in the oxygen reduction reaction at the cathode side of fuel cells.

1 Introduction

Platinum catalysts are essential in applications such as fuel cells. Due to the high cost of Pt, replacements are sought. The use of metal nanoparticles finely dispersed on different types of carbon black (with extremely enlarged surface) leads to a pronounced reduction of the necessary amount of Pt[1]. To further reduce the costs, Ru as a less expensive and more reliable alternative was suggested as catalyst for the oxygen reduction reaction (ORR) at the cathode side of polymer-electrolyte fuel cells (PEFC)[2–4]. Ru-based ORR electro-catalysts modified with Se even feature a superior methanol tolerance[5,6]. Such systems are of particular interest for direct methanol fuel cells in compact mixed reactant geometry (CMR-DMFC) where methanol tolerance is crucial[7,8]. Intense studies of $RuSe_x$-catalysts have been performed[7–10], but their ORR activity is still limited to 70% compared to Pt-based reference materials[9–12].

The optimization of electro-catalysts for oxygen reduction can be brought down to the necessity to tailor a three-phase boundary between the Nafion®-phase (supply of H+), the conductive carbon support (for e− replenishment) and the catalytically active surface of the transition metal as the centre of the catalytic reaction. Hence, there is a soaring interest in characterization techniques capable not only of estimating the overall active surface area of the metallic nanoparticles but also of accounting for particle sizes and shapes, spatial particle distribution and the porosity of the catalyst support.

Information from conventional characterization techniques such as XRD is limited to the average sizes of crystalline particles above 1.5 nm (derived from the Scherrer equation[13]) or to simple size/strain distributions (evaluated by the Warren-Averbach method). Hydrogen and CO chemisorption techniques come to their limits when the stoichiometry is uncertain due to, e.g. the formation of alloyed surfaces or the presence of activity promoters covering an unknown portion of the metallic surface. The electrochemical activity of oxygen reduction catalysts depends to a large extent on the accessible surface area of the metallic nanoparticles and their exposed facets. Conventional TEM is frequently used to characterize nano-particulate catalysts and valuable two-dimensional projected structural information can be extracted from these images. Still, a tool to visualize catalytically active nanostructures as virtual three-dimensional representations easy to perambulate and reliably to evaluate is highly desirable.

Electron tomography represents a powerful characterization technique[14,15] for heterogeneous solid samples[16–19]. Most common are qualitative evaluations[20–22] or manual measurements[23,24] depend-

ing on the personal judgement of the scientist. Recent advances and sophisticated data evaluation extend the field of applications of this technique[25,26] and make it even more attractive for the investigation of heterogeneous catalysts[27–29]. Carbon-supported transition metal catalysts represent a very suited system for such investigations since the contrast between the supporting carbon matrix and the catalytically active metals is sufficiently large[18,30]. The aim of the current contribution is to present a detailed analysis of the size and shape distribution of ruthenium nanoparticles supported on carbon black used as a precursor for the preparation of highly active selenium modified $RuSe_x/C$ ORR-catalysts for the cathode side of PEFCs[31].

Application of conventional reconstruction algorithms yielded tomograms dominated by artefacts. If at all possible, particle extraction by appropriate software required a high degree of the operator's personal judgement which can influence results substantially. The novel DIRECTT algorithm[32] increases the reconstruction quality (in particular regarding the spatial resolution and the absolute contrast scale) tremendously so that the need of image post-processing (filtering) was reduced to a minimum.

New software was developed to create a set of tools to automate the process of evaluating thousands of particles. These programs have been designed with a special emphasis on bringing down the image analysis parameters to very basic properties of the measurements to minimize the possible influence of personal judgement in the analysis. A reliable evaluation of the three-dimensional structure of the catalyst and of the size and shape distribution of ruthenium on the carbon support contributes to the understanding of the fundamental chemical and physical processes that make these types of catalysts so effective.

2 Experimental

2.1 Sample preparation

The commercially available carbon black Vulcan® XC-72R obtained from CABOT Corp[33] was used as starting material to prepare carbon-supported ruthenium nanoparticles. Vulcan® XC-72R represents an industrial standard for conductive carbon blacks and is therefore widely used as a common catalyst support for fuel cells. The specific surface area determined by the BET-method ([34]) is about 230 m^2/g. The specific pore volume evaluated with the BJH-method ([35], incorporating volumes between carbon particles) is 0,62 cm^3/g and 0.066 cm^3/g with the t-plot method ([36], only regarding mesopores but not micropores). $RuCl_3 \cdot xH_2O$ (Sigma-Aldrich®, metal content 35 wt%) was used as Ru precursor for catalyst

preparation (100 mg Vulcan and 71 mg $RuCl_3$ in 200 ml H_2O). All solvents were dried over molecular sieves before precursor solutions of appropriate Ru concentration were prepared. $RuCl_3$ was dissolved in water that had been purged with argon before. The precursor solutions were placed in a round-bottom flask at the end of a quartz tube which was inserted into a split-hinge tube furnace. The resulting suspensions were agitated by ultrasound, after which the solvent was removed by rotary evaporation and the dried catalyst powder was heated under hydrogen at a temperature of 200°C for 30 minutes. The resultant material was rinsed with water to remove all chlorine-containing residues and was finally dried in a desiccator. The investigated carbon-black supported ruthenium particles were prepared as described by [37]. For the preparation of samples suitable for electron tomography, this cloddish powder was dispersed in butanol by ultrasound. The dispersion was then dropped onto a copper grid with a thin carbon foil containing fiducial gold markers (Fig. 1) and dried in a furnace to remove remnants of the butanol.

2.2 Data acquisition and procession

Electron tomography experiments were performed with a Zeiss LIBRA 200FE® transmission electron microscope (TEM) at the Helmholtz Centre Berlin (HZB). Bright-field images were taken at 200 keV while the sample was tilted from -69° to +74° with an angular increment of 1°. X-y-z-tracking[38,39] was done by the Digital Micrograph tomography module (Gatan). The images were aligned by fiducial marker tracking using the software IMOD[40], which revealed that the actual angles of projections differed from the nominal angles as much as 0.2°. Thus, tomographic reconstruction suffers from various limitations (i.e. deviations from ideal complete tomographic data): A limited range of tilt angles, too few projections with respect to the detector size of 2048x2048 pixels, partial opacity caused by some of the gold markers, a non-equidistant set of angles and a problem of the influence of object parts outside the region-of-interest. Conventional reconstruction software does not account well for all these restrictions but the DIRECTT algorithm (Direct Iterative Reconstruction of Computed Tomography Trajectories[32,41]) proved to perform excellently under these conditions. DIRECTT represents a promising alternative to conventional algorithms such as WBP (Weighted Back Projection) or SIRT (Simultaneous Iterative Reconstruction Technique). Instead of back projecting all sinogram values at once, it traces single sinusoidal trajectories in Radon space which are selected from the set of all possible trajectories by criteria such as their angular averaged (filtered) weight or contrast to adjacent trajectories. These reconstruction elements are only

partially added to an intermediate reconstruction. The projection (Radon transform) of this reconstruction is subtracted from the original (i.e. measured) data set in a next step. The obtained residual sinogram is treated in the same way as in the subsequent iteration steps until a pre-selected criterion of convergence is reached. Data pre-processing combined with the advantages of DIRECTT, in particular, extending the reconstruction region beyond that given by the input image size[42], proved to effectively eliminate disturbing streak artefacts.

In the resulting tomogram, each voxel value (grey value) corresponds to the local attenuation coefficient of the specific elements or phases. Each element present in the sample can be assigned to a segment of the tomogram with two appropriate thresholds on the grey values. This step is called 'segmentation' and each segment represents a binarization of the tomogram (e.g. bottom images of Fig. 2).

The ruthenium segment was created applying the Otsu-threshold criterion[43].[†] Therefore, decisions by the operator were not required. Computer analysis of the binarized tomogram segments enabled global measurements concerning ruthenium and carbon and also measurements of each individual ruthenium particle. The digital analysis was carried out with the Insight Toolkit[44] (ITK), the Visualization Toolkit[45] (VTK), octave[46], gnuplot[47] and rendered with Blender[48].

Although the reconstructions have few artefacts, some ruthenium particles, that are very close to each other, are connected because of limited spatial resolution. Therefore, the particles were separated by applying successively two distance map evaluations and a watershed transformation[49,50]. The dependence on the second distance map was introduced to control over- and under-segmentation by ascertained separation and edge uncertainties. The result is more realistic concerning number, size and shape of the ruthenium particles with respect to the original TEM images.

3   Results

We describe the general properties of the catalyst particles in Sec. 3.1. The global measurements of the ruthenium and the carbon segments are presented in Sec. 3.2, followed by an evaluation of the sphericity of the ruthenium particles (Sec. 3.3), showing to which extent a size distribution under the assumption of spherical symmetry (Sec. 3.4) makes sense, motivating further investigations of shape by fitting of ellipsoids (Sec. 3.5 and 3.6). The

---

[†] The Otsu algorithm assumes that the image to be thresholded contains two classes of pixels (e.g. foreground and background) then calculates the optimum threshold separating those two classes so that their combined spread (intra-class variance) is minimal.
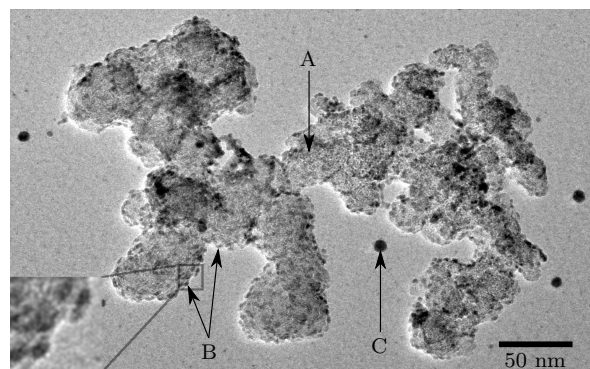

Figure 1: Bright-field TEM image of a catalyst particle
Bright-field TEM image of a catalyst particle showing ruthenium nanoparticles as dark spots supported by a Vulcan® XC-72R carbon black agglomerate. To the right of arrow A the C-particle is more amorphous, while to the left it has a more graphitic character. Arrows B point at ruthenium particles and C to a fiducial marker for the image alignment.

size distribution –although most particles are not spherical (see Fig. 1 and 2)– allows to compare the results with those from other methods such as X-ray diffraction (XRD) and anomalous small-angle X-ray scattering (ASAXS) (Sec. 4) which were based on spherical approximations. After the evaluation of the shapes of the ruthenium particles, the analysis is extended to the local carbon morphology in the vicinity of each ruthenium particle (Sec. 3.6 to 3.8).

3.1   Visual Assessment and 3D Reconstruction

Fig. 1 shows a bright-field TEM image of ruthenium catalyst nanoparticles (small dark spots) distributed over an agglomerate of Vulcan® XC-72 carbon black support (arrow A) deposited on a carbon foil. The carbon particle in Fig. 1 consists mainly of two fractions differing by their appearance and degree of graphitization. Most carbon particles are polycrystalline. As 'degree of graphitization' we designate the fraction of graphitic regions in an otherwise amorphous carbon particle. According to [51], the structural properties of graphitic crystals are described adequately by: crystallite size, crystallite dimension in the a- and c-axis direction and the interlayer spacing. Although the model in Fig. 2 of Ref. 51 shows well-defined monocrystalline regions, the transition from graphitic to amorphous carbon is continuous (see e.g. Fig. 3 of Ref. 51). Therefore, the listed properties are not easily determined. Hence, we use the terms 'more amorphous' and 'more graphitic' to express the tendency of the local carbon structure. The tendency towards more graphitic carbon structure is expressed by a higher ordering of the graphene sheets and a more ball-shaped structure, creating the impression of onion-layers.
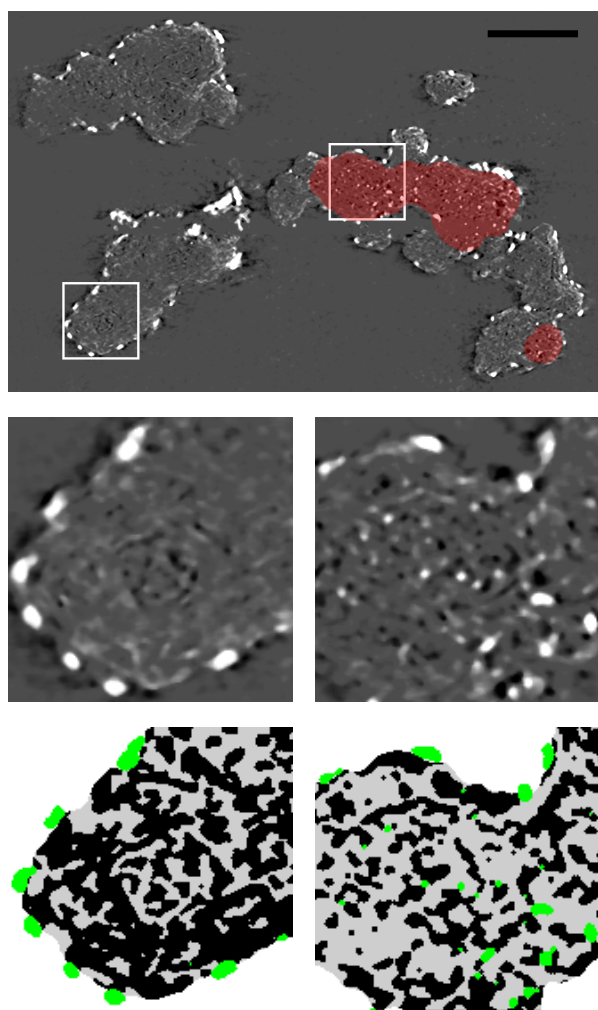
Figure 2: Cross section through the reconstructed tomogram

The upper image shows a cross section through the whole tomogram (contrast-inverted, scale bar 60 nm); red marks the regions that have a more amorphous-like carbon structure, the remaining carbon has a more graphitic character. The middle images show the framed regions of the two different structures in magnification. The result of the segmentation (before watershed separation) is shown in the bottom images.

In Fig. 1, larger branches of onion-like structure with diameters of around 50 nm (mostly on the left side of arrow A) are combined with smaller amorphous-like constituents forming irregular aggregates that vary from 10 nm to 30 nm in width (mostly on the right side of arrow A). The much smaller ruthenium particles range from 1 nm to 5 nm in size (see arrows B and inset) and are spread over the surface of the carbon support. Fiducial gold markers are visible as separate spherical dots on the support foil (arrow C) and were used for image alignment.

Fig. 2 shows a cross section through the median-filtered and segmented tomogram of the sample. The complete tomographic data set consists of many such slices covering the whole reconstructed volume. Most of the ruthenium particles are loc-

ated on the outer surface of the carbon support and are partially embedded. This is typical for onion-like structured carbon regions. Some ruthenium particles can also be found inside the carbon matrix (see images on the right in Fig. 2). These particles are much smaller than those on the surface. However, they can only be found at some locations. This observation is further evaluated in Sec. 3.7

3.2 Volume and surface measures of carbon and ruthenium segments

The different materials (grey values) of the tomogram (see Fig. 2) are assigned to different segments for further investigations. A cross section through the tomogram segments after removal of reconstruction artefacts is shown in the bottom images of Fig. 2: Carbon segment (black), ruthenium segment (green), the pore segment (diameter less than 5 nm, grey) and the surrounding empty space (white) of the tomogram.

The carbon segment

Carbon soot usually used as conductive and inert support for catalytically active metallic nanoparticles is a highly porous material. Since the contrast between carbon and the surrounding empty space is not high and the pores within the carbon matrix can be very small, the representation of the pores is less accurate than the representation of the outer contour of the carbon support.

Voids inside the carbon matrix with wall distances of less than 5 nm were treated as 'pores'. A morphological closing operation[50] was applied to the carbon segment to create a carbon representation without pores. Three small voids inside the carbon are left after the closing operation. More important, the outer surface remains largely unchanged. These two representations enable us to discriminate between outer and inner surface of the carbon structure. Based on this, the carbon support particle in Fig. 1 has a volume of $V_{op} \approx 10.8 \cdot 10^5$ nm^3 (volume with open pores) and a total surface area of $S_{op} \approx 12.3 \cdot 10^5$ nm^2. The closing operation increased the volume by 52% to $V_{cp} \approx 16.4 \cdot 10^5$ nm^3 (volume with closed pores) while the surface decreased to $S_{cp} \approx 2.69 \cdot 10^5$ nm^2. The pore volume then is: $V_p = V_{cp} - V_{op} \approx 5.6 \cdot 10^5$ nm^3; and the corresponding pore surface: $S_p = S_{op} - S_{cp} \approx 9.61 \cdot 10^5$ nm^2. The ratio of the inner surface to the outer surface is $S_p/S_{cp} \approx 3.6$, and the surface-to-volume ratios are: $S_{op}/V_{op} \approx 1.14$ nm^{-1}; $S_{cp}/V_{cp} \approx 0.16$ nm^{-1}. These values are a measure of the surface roughness of the carbon support. The larger the roughness, the more sites there are for ruthenium particles to grow. The less carbon volume is necessary for this, the better the packing of the whole structure with

ruthenium particles. However, a very high packing would be counter-productive since then the ruthenium particles are less likely reached by the reactants during catalysis.

The specific surface area of the carbon deduced from these values, $S_s = S/\varrho_C/V$, lies between 100 m^2/g and 500 m^2/g and the specific pore volume at around $V_s = V_p/\varrho_C/V_{op} \approx 0.23$ cm^3/g.[§]

The ruthenium segment

Before separation (see 2.2, denoted: bs), there are about 2600 particles with a particle volume of at least 64 voxels ≈ 1.12 nm^3. The total Ru volume is: $V_{bs} \approx 1.1 \cdot 10^5$ nm^3 and the surface: $S_{bs} \approx 2.03 \cdot 10^5$ nm^2.

The ruthenium surface not covered by carbon is evaluated by slightly dilating the carbon representation, followed by a conversion of both segments into a mesh representation (see Sec. 3.8). Now, the triangles of the ruthenium surface mesh that do not reside inside the dilated carbon support are regarded as 'uncovered ruthenium surface' (denoted ubs: uncovered, before separation) and is $S_{ubs} \approx 0.74 \cdot 10^5$ nm^2, which is about 36% of the total ruthenium surface S_{bs}. This ratio of uncovered ruthenium surface to total ruthenium surface (Σ) is a key quantity for the effectiveness of the catalyst and will be further discussed in Sec. 4.

After separation (denoted as), there are about 5700 particles (again V > 64 voxels) and a total ruthenium volume of $V_{as} \approx 1.1 \cdot 10^5$ nm^3. Since no voxels are removed by the watershed algorithm chosen, the overall ruthenium volume is not changed. The surface, however, is increased by 11% to $S_{as} \approx 2.25 \cdot 10^5$ nm^2 due to the boundary surface introduced. It is unclear though if this additional surface area is real. Even if, its contribution to catalysis would probably be insignificant because the distance to the nearby particles is too small to allow for good accessibility of this additional surface by the reactants. Therefore, in addition to Σ, we use S_{bs} and S_{ubs} for the calculation of the following values, which we think are important for a comparison with other catalysts of similar type:

- Γ: The amount of uncovered ruthenium surface per unit support surface characterizes the degree of utilization of available support surface,

- Θ: The amount of uncovered ruthenium surface per unit Ru/C catalyst volume can be used for the evaluation of space needed when loading the cathode up to a specific catalytic active surface,

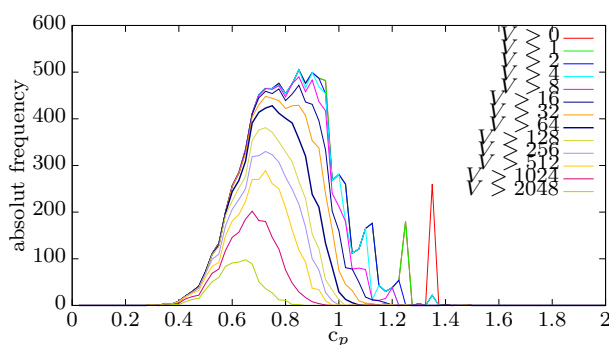- Ξ: The amount of uncovered ruthenium surface related to the mass of the Ru/C catalyst

Figure 3: Sphericity of the ruthenium particles
Histogram plots of the sphericity c_p of the ruthenium particles. Only particles whose volume (in voxel) was bigger than the chosen threshold were considered in the corresponding histogram.

is a more convenient measure when preparing materials for catalyst production.[‡]

For the presented sample:
$\Sigma = S_{ubs}/S_{bs} = 36\%$ (defined before),
$\Gamma = S_{ubs}/S_{op} = 6\%$,
$\Theta = S_{ubs}/(V_{cp} + V_{bs}) = 0.04$ nm^{-1} and
$\Xi = S_{ubs}/(\varrho_C V_{op} + \varrho_{Ru} V_{bs}) = 0.02$ nm^2/g.[§]

3.3 Deviation from spherical symmetry

Most ruthenium particles deviate from spherical shape (see inset in Fig. 1 and Fig. 2). To quantify this, the sphericity $c_p = 6\sqrt{\pi} \; V/S^{3/2}$ of the ruthenium particles was investigated. For a sphere $c_p = 1$, for any other shape $c_p < 1$.

Fig. 3 shows multiple histograms of the sphericity. The histograms differ by their minimum volume threshold. Particles with volumes below this threshold are not included in the corresponding histogram. Values above 1 are caused by errors in the surface estimation of the small particles (see for example[53]). Such particles have to be neglected. Therefore, we restrict our further analysis to particle volumes above 64 voxel.

For any histogram in Fig. 3 with a minimum volume threshold of at least 64 voxel, there are very few particles that are actually spherical ($c_p = 1$). The degree of deviation from spherical shape is much more pronounced than expected from conventional 2D TEM images and as commonly assumed for such metallic nanocrystallites[5]. This suggests fitting ellipsoids to the ruthenium particles

---

[‡]   This is a quantity different from the 'local catalyst loading' as reported by e.g. [52] where the mass of catalyst per support surface area is evaluated. There is no distinction between total and uncovered catalyst surface in the 'local catalyst loading'.

[§]   Using the density of Ru: $\varrho_{Ru} = 12.37$ g/cm^3 and a density of graphite: $\varrho_C = 2.25$ g/cm^{3} [51]. V_{op} and the density of graphite are used because the density of graphite varies less than that of amorphous carbon which would be needed with V_{cp}.
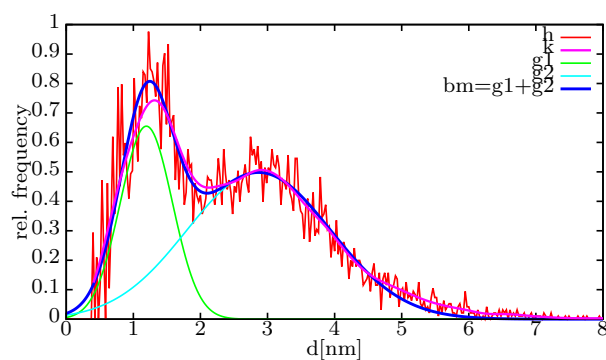
Figure 4: Ruthenium particle size distribution
Histogram showing the distribution of the diameters of all representative ruthenium particles assumed to be spherical.
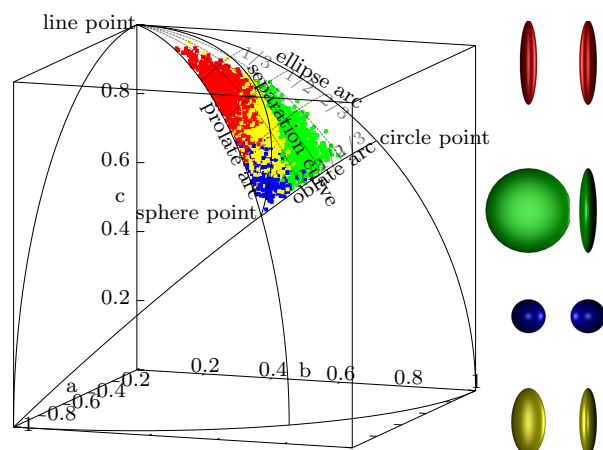

Figure 5: a:b:c-ratios of fitted ellipsoids
Radial projection of the end-points along their point vectors of all a:b:c-ratios onto the unit sphere. The ellipsoids on the side represent the four different types in their extremes (second column: view rotated by 90°).

rather than simple spheres. Generally, it can be assumed that the particles have the form of truncated hexagonal bipyramids because Ru metal crystallizes in a hexagonal closed packed structure[54]. However, the truncated bipyramids are expected to resemble shapes close to ellipsoids if the resolution of the tomographic dataset is insufficient to reveal facets. The shape of the resulting particle representations can range from prolate (cigar-shaped) to oblate (lentil-shaped) depending on the position of the truncation or preferential growth directions. The additional information of the ellipsoid fitting allows to estimate the significance of these influences.

3.4   Ruthenium particle size distribution

The size distribution of the ruthenium particles (Fig. 4) is given as a function of the diameter of a sphere with the same volume as the corresponding particle. The normalized histogram (h) has 300 bins and shows a noisy but distinct bimodal distribution of the particle diameters (particles with $c_p > 1$ were excluded). A kernel density (additive Gaussian functions) distribution plot (k) accounts for the uncertainty of the representation of ruthenium particles. This also reduces the noise and the bimodal distribution becomes more obvious. The distribution was decomposed into two Gaussian functions g1 and g2 centred at $d_1 = 1.2$ nm (variance 0.4 nm) and $d_2 = 2.8$ nm (variance 1.0 nm).

3.5   Shape analysis

Shape analysis is realized by fitting an ellipsoid to each particle after watershed separation. The parameters of the ellipsoid (axes lengths and axes orientations, position in space) are determined by the binary image moments[55,56]. The fitted ellipsoids were scaled to have the same volume as the corresponding particles since this does not change the ratio of the lengths of the main axes: a:b:c (a:b:c-ratio from now on).

These a:b:c-ratios can be regarded as point vectors in 3D space. However, for the evaluation of the shape of each particle, its actual size, i.e. the actual length of the point vector, is of no importance. Therefore, all data points were radially projected onto the unit sphere, as displayed in Fig. 5.

We sorted the axes by their lengths $a < b < c$ which makes the naming distinct. This causes the points to be restricted to a rectangular spherical triangle on 1/48 ($1/8 \cdot 1/6$, for symmetry reasons) of the unit sphere. The points on the triangle arcs correspond to special ellipsoids:

The prolate arc: $a = b < c \Leftrightarrow 1 = a/b < c/b$
The oblate arc: $a < b = c \Leftrightarrow a/b < c/b = 1$
The ellipse arc: $a = 0$

The naming of the axes does not correspond to the common naming in hexagonal systems. Prolate ellipsoids (cigar shape) have a rotational symmetry about the long axis (c), whereas the oblate ellipsoids (lentil shape) have a rotational symmetry about the small axis (a). The corner points of the spherical triangle in Fig. 5 correspond to even more special conditions of the ellipsoids:

The sphere point: $a = b = c$
The circle point: $a = 0 \wedge b = c$
The line point: $a = b = 0$

Exact prolate, oblate and spherical ellipsoids, i.e. with rotational symmetry, solely represent extreme geometrical cases that are unlikely to appear in reality. A large fraction of data points is mapped within significant distance away from the sphere point, indicating that the majority of particles are non-spherical in accordance to the result of Sec. 3.3.

A way to partition all possible ellipsoids into two definite classes is to define the separation condition $a/b = b/c$. Ellipsoids with $a/b < b/c$ are oblate-like, whereas those with $a/b > b/c$ are prolate-like. The
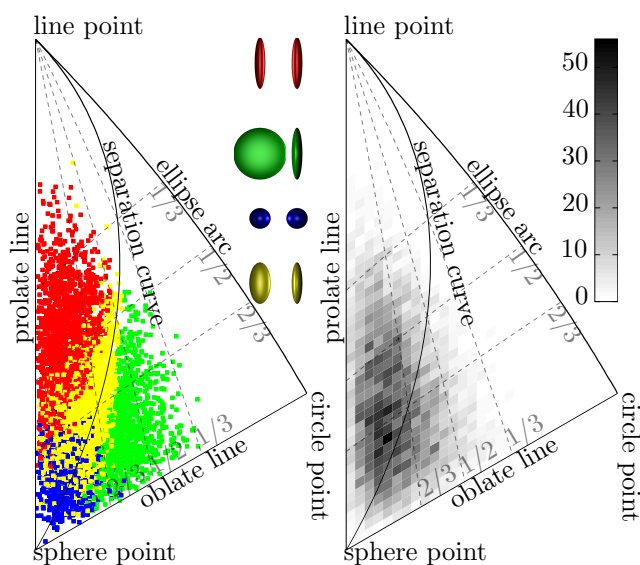
Figure 6: Stereographic projection of a:b:c-ratios and 2D-histogram
a) The stereographic projection of fig. 5.
b) 2D-histogram showing the distribution of the a:b:c-ratios.

condition $a/b = b/c$ corresponds to the case where the eccentricity of the ellipse in the a-b-plane equals the eccentricity of the ellipse in the b-c-plane. This defines the separation curve in Fig. 5.

Each a:b:c-ratio has an error because of the uncertainty in the particle representation. This can be regarded as an error box (not shown) around each point in Fig. 5. If the error permits the shape to be either prolate or oblate (i.e. the error box intersects with the separation curve), the shape is uncertain within the error limits. If, however, the error box includes the sphere point, the ellipsoid can be regarded as spherical within the error limits.

In Fig. 5 the colour of each point corresponds to its ellipsoid type: prolate: red (1783); oblate: green (983); spherical (within error limits, 676): blue; uncertain (within error limits, 2257): yellow. The broken lines ending at the oblate arc mark the corresponding a/b-ratios; those ending on the ellipse arc mark the corresponding b/c-ratios.

This spherical triangle is stereographically[¶] projected (Fig. 6a). The origin of projection was chosen to be the 'sphere point' such that the prolate and the oblate arcs from Fig. 5 are projected onto straight lines.

The true point density cannot be read from Fig. 6a due to overlap of points. The 2D histogram in Fig. 6b visualizes the actual point density distribution of a:b:c-ratios. The grey scale indicates the amount of a:b:c-ratio-points within a field, i.e. the number of particles whose a:b:c-ratios are similar. The fields are not rectangular to avoid underestimation along the 'oblate line'. It is visible that the prolate-like ellipsoids dominate over the oblate-like

---

[¶] The stereographic projection causes less length/area distortion in the projected region than an orthographic projection would.

ones, since the densities in Fig. 6b are higher in the prolate region (red points in Fig. 6a) than in the oblate region (green points in Fig. 6a).

3.6 Spatial distribution of ruthenium particles

We investigated how the studied particles of different shape are distributed in space. For this, each ellipsoid is displayed at the centroid (barycentre or centre of 'mass') of the corresponding particle (Fig. 7).

Most of the spherical ellipsoids (blue) are small (Fig. 7) and are located inside (Fig. 8) the carbon support particle where the carbon seems to be predominantly amorphous (see Fig. 1 and 2). Limited spatial resolution can be a reason for some small particles to appear spherical. However, many other small particles, especially those located on the surface of the carbon support, have a distinct ellipsoidal shape despite their small volume.

This was further evaluated by removing the ellipsoids that are bigger than 2.2 nm³ (128 voxel), which corresponds to a diameter exceeding 1.6 nm, close to the intersection of the two Gaussian functions in Fig. 4. Additionally, ellipsoids within a 5 nm (20 voxel) vicinity of the non-porous representation of the carbon support (grey surface in Fig. 8) were removed as well. Fig. 8 shows that the remaining ellipsoids dominate the right part of the carbon particle which is also the part identified as more amorphous-like by TEM (Fig. 1).

3.7 Local pore density of the carbon support

We analysed the correlation between the density of ruthenium particles inside the carbon support and the apparent carbon structure (crystalline/amorphous) more quantitatively. The approach to distinguish between the two forms makes use of their apparent different porous structure. For each voxel, a local pore density (lpd) was calculated, which is the ratio of the pore volume (pores below 5.2 nm diameter, see bottom images of Fig. 2) to the sum of the pore volume and the carbon volume (disregarding the outside space) within a vicinity sphere of radius R_v around each voxel.

For a vicinity of $R_v \approx 16$ nm, the corresponding lpd_{16} shows a bimodal distribution (Fig. 9). The regions in the tomogram with $lpd_{16} > 0.43$ (black histogram part) were enclosed by a green surface mesh in Fig. 8. These are the regions which correspond to highly porous parts of the carbon particle.

The regions on the right can be assigned to the predominantly amorphous parts which have been identified in 3.1. However, on the left, there is also a region with a high lpd_{16}. This is because the more graphite-like carbon parts can also contain
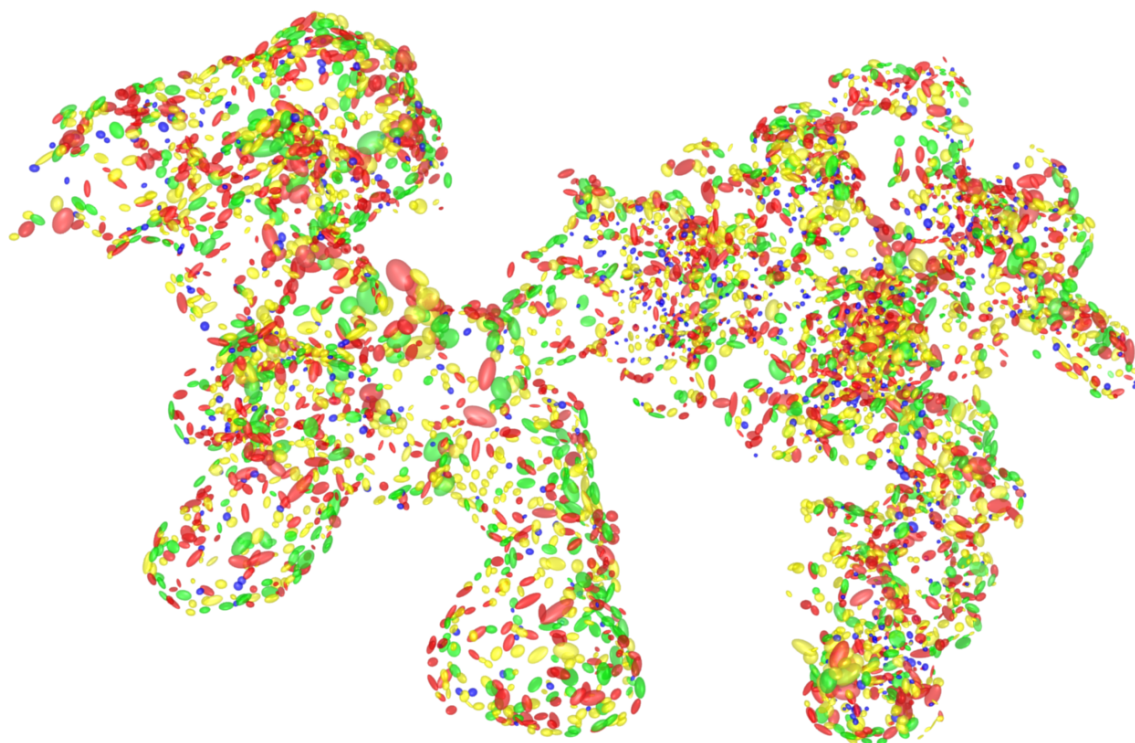
Figure 7: Spatial distribution of the fitted ellipsoids

Green: oblate, red: prolate, yellow: undistinguishable, blue: spherical within the error limits. The particle density is higher on the right side.
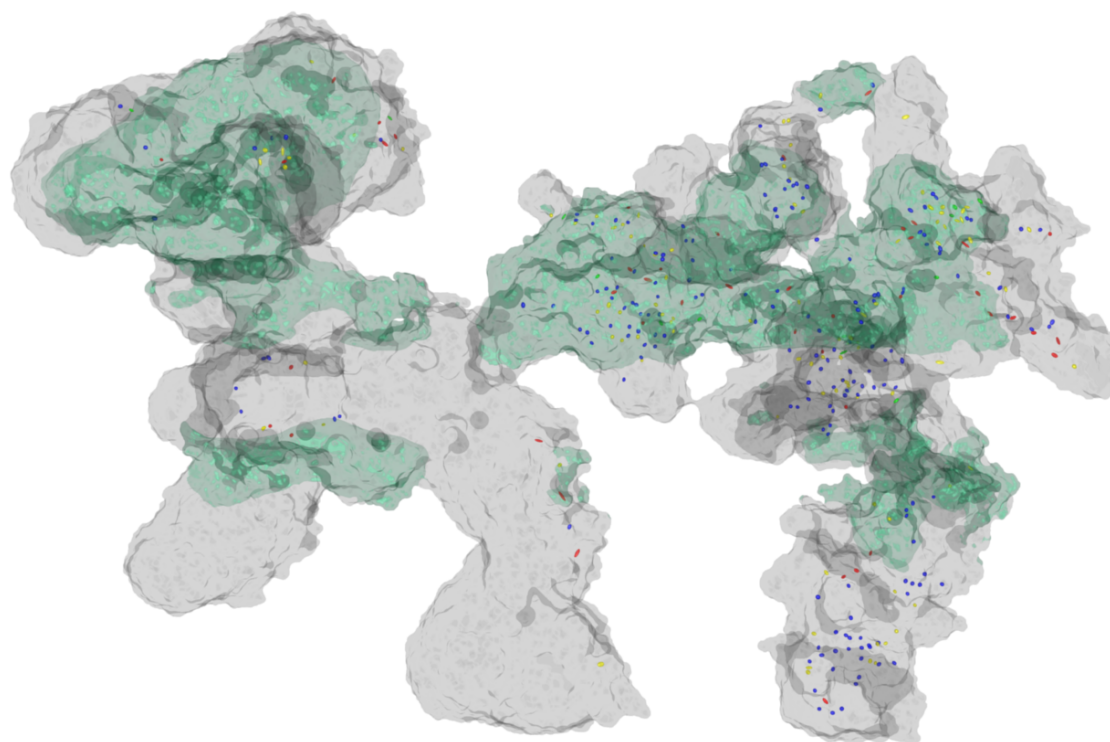

Figure 8: Relation of the inner ruthenium particles to the carbon support

The image shows only the small ellipsoids that are inside the outer carbon surface (grey). Most of the small inner ellipsoids are spherical (blue) and are located in the right side of the support. The light green surfaces enclose regions of the carbon particle with a higher local pore density. These surfaces originate from the thresholded results of the local pore density filter (lpd_{16}) described in Sec. 3.7.
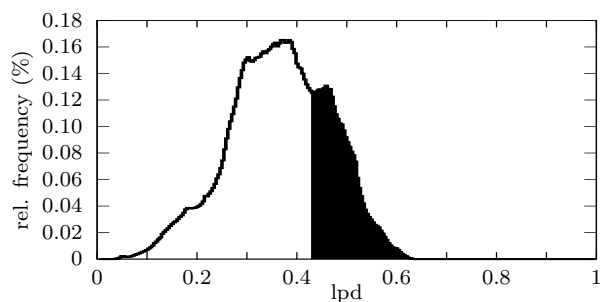
Figure 9: Histogram of the local pore density (lpd_{16})
This lpd_{16} is the local ratio (within a spherical vicinity of 16 nm radius) of the pore volume (pores below 5 nm diameter) to the sum of the pore volume and the carbon volume.

voids in the shape of bent plates between 'onion layers' which dominate the left side of the carbon particle (Fig. 2).

3.8 Orientation of the ruthenium particles on the carbon surface

The fitted ellipsoids not only allow for an evaluation of the particle shape but also for an analysis of the orientation of the ruthenium particles with respect to the carbon support. This can be quantified by the orientation of the mean local surface normal of the carbon support relative to the ellipsoid axes. The voxel representation of the carbon support particle has to be converted to a surface mesh to derive a mean local surface normal. The discrete-marching-cubes algorithm [45,57] in combination with a windowed-sinc-smoothing filter [45,58] was used to create such a mesh representation of the carbon support surface consisting only of triangles. Fig. 10 demonstrates this approach. For the estimation of the local mean normal, the vector sum of triangle normals weighted by their triangle area is calculated. The summation is over all surface triangles of the carbon support that reside inside the ellipsoid. The triangles of the carbon mesh inside the ellipsoid are highlighted in Fig. 10. The direction of the mean surface normal is indicated by the line originating from the centre of the ellipsoid. Note that triangles not visible in Fig. 10 also contribute to the normal calculation.

The upper image in Fig. 10 shows that this estimation can be inappropriate if the ellipsoid only encloses very few triangles of the carbon surface. The ellipsoid was inflated by about 1 nm in all directions to improve the estimation (see lower image in Fig. 10). After this inflation, many more triangles are considered in the calculation of the mean local carbon surface normal. It only makes sense to consider ellipsoids near the carbon surface, i.e. that intersect with the smoothed mesh of the carbon surface.

Finally, the orientation of the local surface normal relative to the axes of the ellipsoid can be eval-
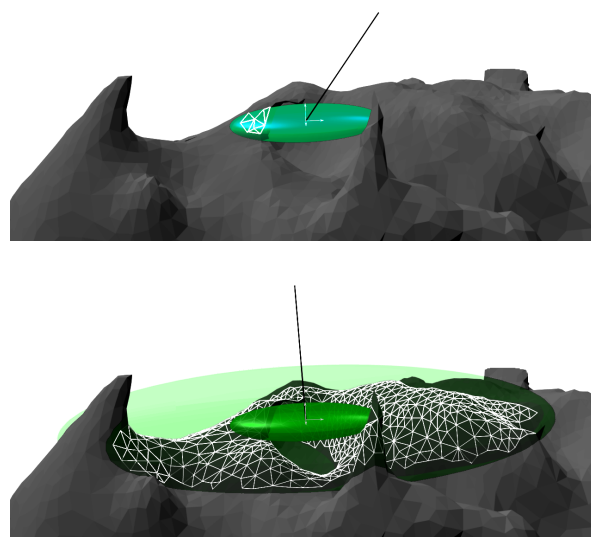

Figure 10: Determination of a local surface normal of the carbon support (schematic)
Upper image: A fitted ellipsoid representing a non-spherical ruthenium particle on the surface of the carbon support and the local carbon surface normal (black line).
Lower image: The ellipsoid and an up-scaled one (transparent). The triangles contributing to the surface normal calculation increased significantly yielding a more appropriate estimation of the average surface normal.

uated. A graphical visualisation of these results can be obtained by regarding the orientation of the local surface normal as a point on the unit sphere. The coordinate system implied by the ellipsoid's axes can be chosen such that all angles are $\leq 90°$. This makes the points of all local normals lie within the spherical triangle of the first quadrant and allows to combine the data in a single plot. Fig. 11 shows the stereographic projection (along [111]) of this quadrant. As before, the point density is visualized by a 2D-histogram. The corners of the projected spherical triangle correspond to the directions of the ellipsoid axes.

Most particles are oriented in such a way that the local surface normals of the carbon support point along the a-axis which is by definition the smallest of the ellipsoid's axes. As a preliminary conclusion, this means that most particles stick to the carbon in such a way that they are in a potential minimum of the attractive forces of the carbon surface, i.e. they stick to the carbon support with their least curved ('flattest') side. For a nearly even surface this also means that the contact area of the slightly embedded particles to the carbon surface is maximized, as generally expected.

However, the 2D-histogram in Fig. 11 shows a significant deviation from the expected radial distribution around the a-axis point in the top corner. A larger fraction of particles can be found along the arc connecting the a-axis and the b-axis (see inset
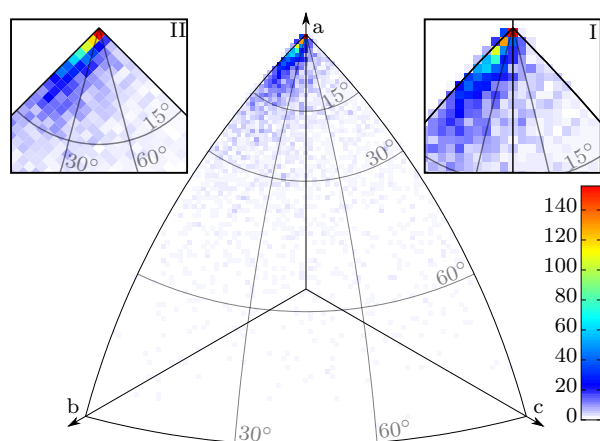
Figure 11: Orientation tendency of the ellipsoids to the local support surface
Inlay I and II show the region around the a-axis magnified by two. Inlay II: As most points are close (up to 15°) to the a-axis [100] it is sensible to project stereographically along [100]. This allows to circumvent the under sampling of the histogram fields along the edges.

II in Fig. 11). This suggests that a statistically significant number of particles not only contact the carbon support with their largest side but also with the next smaller side. Such cases can be explained by particles aligned along steps of graphene layers on the outer surface of the carbon support (as will be explained in Fig. 12).

4 Discussion

The presented methods provide a very detailed insight into the morphology of the samples studied and allow to draw conclusions about important processes taking place during production but also during catalysis. The methods of digital image analysis developed are not restricted to TEM tomography but could also be applied to any 3D tomographic dataset, e.g. obtained by X-ray tomography.

Carbon-supported ruthenium nanoparticles may be used to catalyse the oxygen reduction reaction at the cathode side of fuel cells. However, their catalytic activity for this reaction can be significantly enhanced by decorating the surface of the ruthenium particles with Se. This yields a catalyst with commercial significance. As the structure predetermined by Ru/C can be analysed unambiguously by TEM tomography, the results should also be valid for $RuSe_x/C$ catalysts since selenization does not alter the material's morphology above the resolution limit of TEM tomography[5]. Thus, we used a Se-free Ru/C intermediate which represents the final morphology despite the simplification.

Neutron activation analysis (NAA) yields a mass ratio of ruthenium to carbon of $m_{Ru}/m_C = 20.6\%$.

This is equivalent to a volume ratio$^{\parallel}$ of V_{Ru}/V_C ranging from 3.3% to 4.2%; the same ratio evaluated from the tomogram ranges from 3.7% to 28% (determined by erosion and dilation of the segments).

The specific surface area of the used carbon evaluated by the BET-method (230 m^2/g) lies within the range determined by electron tomography (S_s ranging from 100 m^2/g to 500 m^2/g). Values for the specific surface area of Vulcan reported in literature range from around 100 m^2/g to 300 m^2/g.[59] The higher limit for S_s derived from electron tomography is reasonable taking into account that Vulcan carbon particles exhibit also highly porous parts (see Sec. 3.7) which are comparable to 'Black Perl' carbon (whose specific surface area reaches up to about 1500 m^2/g[59]). Depending on the amount of highly porous regions within a carbon particle, the value for S_s determined by electron tomography will vary in regard to that of integral methods such as BET.

The specific pore volume evaluated by the BJH-method (0,62 cm^3/g) also incorporates volumes between carbon particles whereas the t-plot method (0.066 cm^3/g) only regards mesopores but not micropores. The specific pore volume derived from electron tomography ($V_s \approx 0.23$ cm^3/g) lies in between because only pores below 5 nm including micropores are regarded.

TEM tomography shows that most ruthenium particles are formed on the outer surface of the carbon support particles. The carbon support has different structures within it, one is more amorphous and the other more graphitic in character. These two carbon structures affect the formation of the ruthenium particles. The ruthenium particles have a preference to grow on the outer surface, but in the amorphous parts small ruthenium particles also exist inside the support.

Most ruthenium particles are found on the outer surface although the inner surface is about 3.6 times larger than the outer surface. This is due to the limited or restricted supply of $RuCl_3$ during the formation process of the ruthenium particles: $RuCl_3$ solution can penetrate deep into the pore system of the amorphous carbon because it has shorter and more direct connections to the outer surface (see Fig. 2). The pores found in this regions are comparable with types (c) (d) (e), sketched in the schematic cross section in Fig. 1 of Ref. 60. The pores or cavities (like type (a) in Ref. 60) in the more graphitic regions –the regions that are like layers of onions– have little or no direct connections to the outer surface which prevents the $RuCl_3$ solution from penetrating deep into this pore system.

$^{\parallel}$ Using the density of Ru: $\varrho_{Ru} = 12.37 g/cm^3$ and the density of graphite ϱ_C ranging from 2.0 g/cm^3 to 2.5 g/cm^3. The density of graphite is used because the pore volume is not included in the ratio calculation from the tomogram measurements.
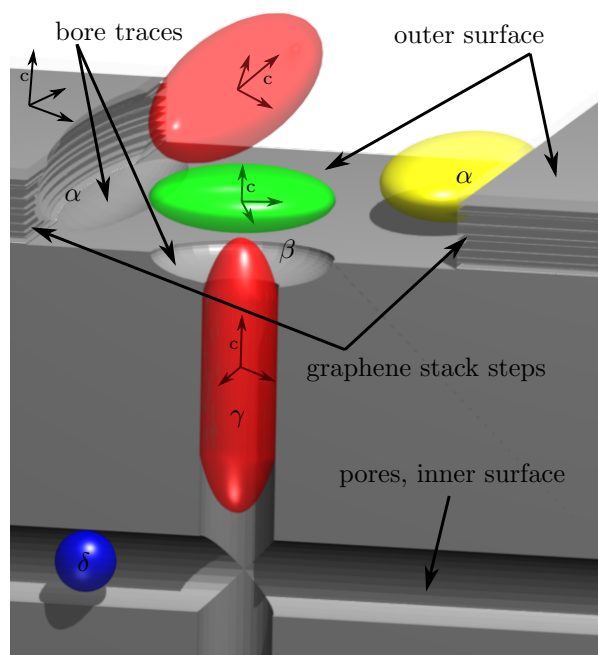
Figure 12: Schematic image of the ruthenium particle positions

Schematic cut-out of the structure to visualize the idealized positions of ruthenium particles related to features of the carbon support. Ruthenium particles are represented by their most likely type of fit-ellipsoid coloured according to Fig. 6. The particle positions at a step of a stack of graphene layers is marked by α. Pores can be closed (position β) by oblate or prolate particles or a combination of the two types. Particles inside pores close to the outer surface (position γ) can grow until their shape is restricted by the pore. Particle positions deep inside the pore system are denoted by δ. Two ellipsoids are slightly lifted from the surface to reveal their embedding/bore traces in the carbon. Local *crystallographic* coordinate systems are drawn for some ruthenium particles and graphite.

Supply of RuCl$_3$ solution is important for the formation of ruthenium particles. If the supply in the pores is limited or even ceases, because the connection to the RuCl$_3$ reservoir is blocked by precipitation of the liquid close to the entries of micropores, the number of ruthenium particles formed after hydrogen treatment is limited and the particle shape is then defined by the size and the geometry of the micropore (see Fig. 12). Therefore, the particles that form inside the pore system (blue ellipsoid in Fig. 12) cannot grow as much as the particles on the outer surface. Furthermore, only very few particles can grow in the more graphitic regions since the pore system here has even fewer connections to the outer RuCl$_3$ supply. This explains why only very few ruthenium particles are inside the part left of arrow A (Fig. 1) despite the high *lpd*, but also why the ruthenium particles in the more amorphous part on the right are small.

Hence, the large inner surface of the carbon support contains fewer ruthenium particles than the outer surface and therefore the inner surface and its ruthenium particles contribute less to the over-

all catalytic effectiveness of the material. In other words, the increase of the surface-to-volume ratio by the inner surface (from 0.16 nm^{-1} to 1.14 nm^{-1}) has less effect than an increase of the ratio by additional outer surface would have. Space in the pores is too restricted (i.e. the pore volume is too small) for the pore system to have the same importance on catalysis as the outer structure. This holds with respect to the amount of catalytic sites but also regarding the accessibility of these sites by the reactants.

One third of the total ruthenium surface has no interface with the carbon support. One explanation for this low amount is the confinement of the particles inside the pores and the partial embedding of the outer particles into the carbon support (see Fig. 12). This means that only one third of the total surface of the ruthenium particles present in the investigated sample can contribute to the catalytic active surface in the process of the oxygen reduction reaction at the cathode side in a fuel cell. This result can tentatively be explained by particle formation as a result of the interaction of the RuCl$_3$ precursor adsorbed on the carbon surface and the subsequent reduction of it by hydrogen. Nucleation of metal particles is most likely to take place in pores and along steps/kink sites of graphene layers at the outer surface of the carbon support. Homogeneous nucleation can be expected in amorphous cavities of the carbon support. Formation of (001), (100), (011) and facets of equivalent symmetry is most likely due to their low surface energies [54]. These crystallites have the shape of truncated hexagonal bipyramids occasionally combined with the facets of a hexagonal prism. Most projections of such nanoparticles are nearly spherical under limited resolution as reported by [54]. Elongated particles are expected to grow preferentially along the hcp c-axis of metallic ruthenium. We assume that they grow either along micropores (position γ in Fig. 12, generally oriented in the [001] direction of the graphite, i.e. perpendicular to graphene layers) or along steps of graphene stacks on top of the graphite substrate (position α in Fig. 12, c-axis of the metallic ruthenium perpendicular to the [001] direction of the graphene layers). Particles at position α in Fig. 12 would explain the spread towards the b-axis in Fig. 11. Not only the 'flattest' side touches the carbon support but also the 'next flattest' side, which sticks to the step of a stack of graphene layers. Particles that nucleate on top of micropore entries (position β in Fig. 12) presumably form tabular ellipsoids by interaction of the (001) ruthenium facet with the graphene surface (epitaxial orientation).

The two thirds of the ruthenium surface that touch the carbon support are also important since electrons have to be conducted from the carbon support to the ruthenium particle during catalysis in the fuel cell. The larger the contact area of the ru-

thenium particles to the carbon support, the higher is the conductance. We therefore expect the quantity Σ (the ratio of uncovered to total ruthenium surface) to possess an optimal value. If Σ is close to 0, the amount of uncovered ruthenium surface is low and limits catalytic activity, if Σ is close to 1, catalytic activity is limited due to insufficient conduction of electrons. Further experiments would be necessary to find out if $\Sigma = 0.36$ is close to the optimal value.

The ruthenium particle size distribution, assuming spherical symmetry, yields two diameters, the larger one at 2.8 nm with a variance of 1 nm. This result is comparable to the diameters evaluated by other methods: ASAXS[11]: 2.5 nm; XRD[11]: 2.2 nm; BF-TEM: 3±1 nm. If only one Gaussian function (as for ASAXS and XRD) is fitted to the size distribution in Fig. 3.4 the resulting mean diameter is about 2.5 nm. We explain the slightly higher estimate from TEM images by the actual deviation from spherical symmetry and the fact that isotropically oriented ellipsoidal particles generally appear bigger in a projection than the diameter estimated by an equal volume approach (as in Fig. 3.4). In addition, particle selection by a scientist tends to lead to a choice of larger particles since smaller ones are more easily overlooked.

As any deviation of the ruthenium particles from spherical shape increases their surface-to-volume ratio, more surface is available for catalysis without an increase in material. The result is a more effective catalyst at the same material costs.

Particle shape analysis based on an approximation by ellipsoids shows that most particles (about 40% of 5700) have an undefined shape, i.e. neither prolate, oblate nor spherical. However, there are about twice as many prolate particles as oblate particles (prolate:oblate = 2:1). This ratio is not affected much by the separation procedure (without separation it is 936:422) nor is the number of spherical particles increased significantly (412 before and 676 after separation). The shape of the ruthenium particles can be an indicator for preferential growth directions that can lead to differently sized and oriented facets. These preferential growth directions can be along edges of graphene layers on the outer surface or along pores of the support material (see Fig. 12). Metallic hcp-Ru nanoparticles usually expose surfaces with different crystallographic orientation to the chemical reactants, likely featuring different catalytic activity depending on the size and orientation of the facets. Therefore, the ratio between prolate and oblate nanoparticles should be considered as one factor influencing the overall catalytic activity.

The ruthenium particle representations are expected to be affected by the 'missing wedge'[61] which causes an artificial elongation of the ruthenium particle representation. This will result in a tendency towards prolate ellipsoids in the shape analysis. Therefore, the actual ratio of prolate to oblate-shaped particles will be more balanced than 2:1 (result from Sec. 3.5). However, an actual deviation from spherical symmetry is definitely present due to the significant number of oblate particles. The effect of the missing wedge on spherical particles would only lead to prolate particle representations. Additionally, the fact that in most cases the a-axis of the ellipsoid is aligned parallel to the local surface normal (see Sec. 3.8) rules out a significant effect of the missing wedge in the DIRECTT reconstruction. An elongation of the particles caused by the missing wedge would not be isotropic but only along one global axis which is in conflict with the result obtained by the local alignment analysis (Sec. 3.8) since the orientation of the local carbon surface normal can be expected to be isotropic.

5 Conclusions

We have demonstrated that TEM tomography can provide a quantitative structure analysis of catalytically active ruthenium nanoparticles supported by carbon. The size distribution of the ruthenium particles is bimodal. Particles from the smaller mode are formed preferentially within the more amorphous parts of the support, whereas larger particles are formed on the outer surface of the support. Fitting ellipsoids to the individual particles reveals that most particles are not spherical and the ratio of prolate to oblate particle numbers is about 2:1. The analysis of the alignment of the ruthenium particles with respect to the local support surface suggests that prolate particles presumably form along the edges of graphene sheets on the support or grow along pores. One factor influencing the overall catalytic activity is the ratio between prolate and oblate nanoparticles since it can indicate preferential growth directions which lead to differently sized facets. Thus, TEM tomography has proven to yield valuable information about the distinct nanostructure of different classes of catalytically active particles in general. Their individual contribution to the overall catalytic activity should be considered in further investigations to optimise the oxygen reduction performance of, e.g. carbon-supported selenium modified ruthenium catalysts ($RuSe_x/C$).

6 Acknowledgement

References

[1] S. Srinivasan, E. Ticianelli, C. Derouin and A. Redondo, *Journal of Power Sources*, 1988, **22**, 359 – 375.

[2] N. Alonso-Vante, H. Tributsch and O. Solorza-Feria, *Electrochimica Acta*, 1995, **40**, 567–576.

[3] V. Trapp, P. Christensen and A. Hamnett, *Journal of the Chemical Society, Faraday Transactions*, 1996, **92**, 4311–4319.

[4] F. J. Rodríguez, P. J. Sebastian, O. Solorza and R. Pérez, *International Journal of Hydrogen Energy*, 1998, **23**, 1031–1035.

[5] G. Zehl, P. Bogdanoff, I. Dorbandt, S. Fiechter, K. Wippermann and C. Hartnig, *Journal of Applied Electrochemistry*, 2007, **37**, 1475–1484.

[6] K. Wippermann, B. Richter, K. Klafki, J. Mergel, G. Zehl, I. Dorbandt, P. Bogdanoff, S. Fiechter and S. Kaytakoglu, *Journal of Applied Electrochemistry*, 2007, **37**, 1399–1411.

[7] D. C. Papageorgopoulos, F. Liu and O. Conrad, *Electrochimica Acta*, 2007, **52**, 4982 – 4986.

[8] A. E. Comyns, *Focus on Catalysts*, 2007, 10.1016/S1351–4180(07)70248–9.

[9] N. Alonso-Vante, *Fuel Cells*, 2006, **6**, 182–189.

[10] D. Cao, A. Wieckowski, J. Inukai and N. Alonso-Vante, *Journal of the Electrochemical Society*, 2006, **153**, A869–A874.

[11] G. Zehl, G. Schmithals, A. Hoell, S. Haas, C. Hartnig, I. Dorbandt, P. Bogdanoff and S. Fiechter, *Angewandte Chemie, International Edition*, 2007, **46**, 7311–7314.

[12] S. Fiechter, I. Dorbandt, P. Bogdanoff, G. Zehl, H. Schulenburg and H. Tributsch, *Journal of Physical Chemistry C*, 2007, **111**, 477–487.

[13] S. F. Bartram, in *Handbook of X-Rays*, ed. E. F. Kaelble, McGraw-Hill, New York, 1967, ch. 17, pp. 17.1–17.18.

[14] J. Frank, *Electron Tomography: Methods for Three-Dimensional Visualization of Structures in the Cell*, Springer, Berlin, 2nd edn., 2006, p. 455.

[15] *Advanced Tomographic Methods in Materials Research and Engineering*, ed. J. Banhart, Oxford University Press, 2008, pp. 1–480.

[16] C. Kübel, A. Voigt, R. Schoenmakers, M. Otten, D. Su, T.-C. Lee, A. Carlsson and J. Bradley, *Microscopy and Microanalysis*, 2005, **11**, 378–400.

[17] H. Friedrich, J. R. A. Sietsma, P. E. de Jongh, A. J. Verkleij and K. P. de Jong, *Journal of the American Chemical Society*, 2007, **129**, 10249–10254.

[18] H. Friedrich, P. E. de Jongh, A. J. Verkleij and K. P. de Jong, *Chemical Reviews*, 2009, **109**, 1613–1629.

[19] P. A. Midgley and R. R. Dunin-Borkowski, *nature materials*, 2009, 271–280.

[20] P. A. Midgley, M. Weyland, J. M. Thomas, P. L. Gai and E. D. Boyes, *Angewandte Chemie*, 2002, **114**, 3804–3807.

[21] M. Weyland, P. A. Midgley and J. M. Thomas, *Journal of Physical Chemistry B*, 2001, **105**, 7882–7886.

[22] S. Hata, K. Kimura, H. Gao, S. Matsumura, M. Doi, T. Moritani, J. S. Barnard, J. R. Tong, J. H. Sharp and P. A. Midgley, *Advanced Materials*, 2008, **20**, 1905–1909.

[23] H. Rösner, T. Scherer and G. Wilde, *Scripta Materialia*, 2009, **60**, 168–170.

[24] L. C. Gontard, R. E. Dunin-Borkowski, R. K. K. Chong, D. Ozkaya and P. A. Midgley, *Journal of Physics: Conference Series*, 2006, **26**, 203–206.

[25] M. Shirai, K. Tsumori, M. Kutsuwada, K. Yasuda and S. Matsumura, *Nuclear Instruments and Methods in Physics Research Section B: Beam Interactions with Materials and Atoms*, 2009, **267**, 1787 – 1791.

[26] H. Rösner, S. Parida, D. Kramer, C. A. Volkert and J. Weissmuller, *Advanced Engineering Materials*, 2007, **9**, 535–541.

[27] H. Friedrich, S. Guo, P. E. de Jongh, X. Pan, X. Bao and K. P. de Jong, *ChemSusChem*, 2011, n/a–n/a.

[28] C. Kübel, D. Niemeyer, R. Cieslinski and S. Rozeveld, THERMEC 2009, 2010, pp. 2517–2522.

[29] E. P. W. Ward, T. J. V. Yates, J. J. Fernandez, D. E. W. Vaughan and P. A. Midgley, *Journal of Physical Chemistry C*, 2007, **111**, 11501–11505.

[30] R. Grothausmann, I. Manke, G. Zehl, I. Dorbandt, P. Bogdanoff, S. Fiechter, M. P. Hentschel, A. Lange, A. Kupsch, A. Hilger and J. Banhart, *MP Materials Testing*, 2010, **52**, 706–711.

[31] K. S. Nagabhushana, E. Dinjus, H. Bonnemann, V. Zaikovskii, C. Hartnig, G. Zehl, I. Dorbandt, S. Fiechter and P. Bogdanoff, *Journal of Applied Electrochemistry*, 2007, **37**, 1515–1522.

[32] A. Lange, M. P. Hentschel and A. Kupsch, *MP Materials Testing*, 2008, **50**, 272–277.

[33] Cabot, *Vulcan XC-72R*, Cabot Corporation, 2002.

[34] S. Brunauer, P. H. Emmett and E. Teller, *Journal of the American Chemical Society*, 1938, **60**, 309–319.

[35] E. P. Barrett, L. G. Joyner and P. P. Halenda, *Journal of the American Chemical Society*, 1951, **73**, 373–380.

[36] B. C. Lippens and J. H. de Boer, *Journal of Catalysis*, 1965, **4**, 319 – 323.

[37] G. Zehl, I. Dorbandt, G. Schmithals, J. Radnik, K. Wippermann, B. Richter, P. Bogdanoff and S. Fiechter, *ECS Transactions*, 2006, **3**, 1261–1270.

[38] A. Koster, A. V. den Bos and K. van der Mast, *Ultramicroscopy*, 1987, **21**, 209 – 222.

[39] A. Koster, W. de Ruijter, A. V. D. Bos and K. V. D. Mast, *Ultramicroscopy*, 1989, **27**, 251 – 272.

[40] J. R. Kremer, D. N. Mastronarde and J. R. McIntosh, *Journal of Structural Biology*, 1996, **116**, 71–76.

[41] A. Lange, A. Kupsch, M. P. Hentschel, I. Manke, N. Kardjilov, T. Arlt and R. Grothausmann, *Journal of Power Sources*, 2011, **196**, 5293 – 5298.

[42] M. P. Hentschel, A. Lange, A. Kupsch and B. R. Müller, *MP Materials Testing*, 2010, **52**, 668–675.

[43] N. Otsu, *IEEE Transactions on Systems, Man and Cybernetics*, 1979, **9**, 62–66.

[44] ITK development team, *ITK*, open source, 3.18, http://www.itk.org.

[45] VTK development team, *VTK*, open source, 5.4, http://www.vtk.org.

[46] J. W. Eaton *et al.*, *Octave*, open source, 3.0.5, http://www.gnu.org/software/octave/.

[47] T. Williams, C. Kelley *et al.*, *gnuplot*, open source, 4.4, http://gnuplot.sourceforge.net/docs_4.4/gnuplot.pdf.

[48] Blender Foundation, *Blender*, open source, 2.49, http://www.blender.org.

[49] R. Beare and G. Lehmann, *Insight Journal*, 2006.

[50] P. Soille, *Morphological Image Analysis: Principles and Applications*, Springer, 2nd edn., 2004, p. 391.

[51] M. Wissler, *Journal of Power Sources*, 2006, **156**, 142 – 150.

[52] P. A. Midgley, J. M. Thomas, L. Laffont, M. Weyland, R. Raja, B. F. G. Johnson and T. Khimyak, *Journal of Physical Chemistry B*, 2004, **108**, 4590–4592.

[53] J. Ziegel and M. Kiderlen, *Image and Vision Computing*, 2010, **28**, 64–77.

[54] R. M. Nielsen, S. Murphy, C. Strebel, M. Johansson, I. Chorkendorff and J. H. Nielsen, *Journal of Nanoparticle Research*, 2010, **12**, 1249–1262.

[55] G. Lehmann, *Insight Journal*, 2008.

[56] D. Padfield and J. Miller, *Insight Journal*, 2008.

[57] W. E. Lorensen and H. E. Cline, *Computer Graphics*, 1987, **21**, 163–169.

[58] *The VTK User's Guide*, ed. W. J. Schroeder, Kitware, Inc., 11th edn., 2010, pp. 1–528.

[59] K. Kinoshita, *Carbon: Electrochemical and Physicochemical Properties*, Wiley & Sons, 1988, pp. 1–560.

[60] J. Rouquerol, D. Avnir, C. W. Fairbridge, D. H. Everett, J. M. Haynes, N. Pernicone, J. D. F. Ramsay, K. S. W. Sing and K. K. Unger, *Pure and Applied Chemistry*, 1994, **66**, 1739 – 1758.

[61] M. Radermacher, *Journal of Electron Microscopy Technique*, 1988, **9**, 359–394.

1
2
3
4
5
6
7
8
9
10
11
12
13
14
15
16
17
18
19
20
21
22
23
24
25
26
27
28
29
30
31
32
33
34
35
36
37
38
39
40
41
42
43
44
45
46
47
48
49
50
51
52
53
54
55
56
57
58
59
60